Faculty Publications, Department of Physics and Astronomy

Research Papers in Physics and Astronomy

2-1-2023

Chiral photocurrent in a Quasi-1D TiS3 (001) phototransistor

Simeon J. Gilbert

Mingxing Li

Jia-Shiang Chen

Hemian Yi

Alexey Lipatov

See next page for additional authors

Authors

Simeon J. Gilbert, Mingxing Li, Jia-Shiang Chen, Hemian Yi, Alexey Lipatov, Jose Avila, Alexander Sinitskii, Maria C. Asensio, Peter A. Dowben, and Andrew J. Yost

PAPER

Chiral photocurrent in a Quasi-1D TiS$_3$ (001) phototransistor

View the article online for updates and enhancements.

You may also like

Chiral photocurrent in a Quasi-1D TiS$_3$ (001) phototransistor

Simeon J Gilbert[1] , **Mingxing Li**[2], **Jia-Shiang Chen**[2], **Hemian Yi**[3], **Alexey Lipatov**[4] , **Jose Avila**[3], **Alexander Sinitskii**[4] , **Maria C Asensio**[5] , **Peter A Dowben**[1] and **Andrew J Yost**[6,7,*]

[1] Department of Physics and Astronomy, University of Nebraska-Lincoln, Lincoln, NE 68588-0299, United States of America
[2] Center for Functional Nanomaterials, Brookhaven National Laboratory, Upton, NY 11973, United States of America
[3] Synchrotron SOLEIL and Université Paris-Saclay, L'Orme des Merisiers, BP48, 91190 Saint-Aubin, France
[4] Department of Chemistry, University of Nebraska-Lincoln, Lincoln, NE 68588-0304, United States of America
[5] Materials Science Institute of Madrid (ICMM), Spanish Scientific Research Council (CSIC), and MATINÉE: the CSIC Research Associated between the Institute of Materiasl Sciences of the Valencia University (ICMUV) and the ICMM, Cantoblanco, E-28049 Madrid, Spain
[6] Department of Physics, Oklahoma State University, Stillwater, OK 74078-3072, United States of America
[7] Oklahoma Photovoltaic Research Institute, Oklahoma State University, Stillwater, OK, United States of America

E-mail: andrew.yost@okstate.edu

Abstract

The presence of in-plane chiral effects, hence spin–orbit coupling, is evident in the changes in the photocurrent produced in a TiS$_3$(001) field-effect phototransistor with left versus right circularly polarized light. The direction of the photocurrent is protected by the presence of strong spin–orbit coupling and the anisotropy of the band structure as indicated in NanoARPES measurements. Dark electronic transport measurements indicate that TiS$_3$ is n-type and has an electron mobility in the range of 1–6 cm^{2}V^{-1}s^{-1}. I–V measurements under laser illumination indicate the photocurrent exhibits a bias directionality dependence, reminiscent of bipolar spin diode behavior. Because the TiS$_3$ contains no heavy elements, the presence of spin–orbit coupling must be attributed to the observed loss of inversion symmetry at the TiS$_3$(001) surface.

Supplementary material for this article is available online

(Some figures may appear in colour only in the online journal)

---

* Author to whom any correspondence should be addressed.

1. Introduction

Spin-polarized photocurrents have been predicted for transition metal *di*chalcogenides (TMDs) [1–4] and there are indications that circularly polarized light can create spin selective excitations in monolayer TMDs, due to large spin–orbit coupling in these systems. For example, polarized photoluminescence appears in atomically thin MoS_2 when excited by circularly polarized light, whereas the photoluminescence is not polarized in bilayer MoS_2 [5]. Xie and Cui created a spin-polarized photocurrent in WS_2 and detected the polarization using a lateral spin-valve [6]. Spin polarized photocurrents in high Z materials is not unexpected but it would be unusual in low Z materials, as spin–orbit coupling is generally not significant for materials with Z less than Cu [7]. For sensor and device applications, the TMDs are far from ideal however.

In reality, few materials are perfect and in the limit of the very small, imperfections can have disastrous effects, especially on device performance in say a transistor. For example, it has become evident that edge functionalization can have a profound effect on transport in 2D materials [8]. The great advantages of graphene, i.e. its low electron effective mass and high carrier mobility, are lost when conduction channel widths shrink so much that the band gap opening associated with the size reduction below 50 nm is accompanied by an increase in electron effective mass [9, 10] and a loss in carrier mobility [8, 11–13]. These edge scattering effects will also dominate the TMDs, with MX_2 composition (M=Mo, W; X=S, Se, Te), with the additional complexity that edge states will make these materials less semiconducting by 'filling in' the band gap [14, 15]. It is predicted that transition metal *tri*chalcogenides (TMTs) offer several interesting new aspects. TMTs from the MX_3 and the In_4X_3 (M=Ti, Zr, Hf; X=S, Se, Te) class of materials contain van der Waals-like bound 2D layers, i.e. weak interlayer adhesion, which are similar to the layered structure of TMDs with weak interlayer van der Waals interactions and strong intralayer covalent interaction [16–19]. As with TMDs [20–23], the layers of single crystal TMTs can be mechanically or chemically exfoliated to produce single- and few-layer sheets for electrical and optical measurements [16–18, 24–41]. However, while 2D layers of TMDs are relatively isotropic, layers of TMTs are strongly anisotropic [41–43], which can be advantageous.

Recent studies [16, 18, 27] have shown that the MX_3 TMTs are formed from one-dimensional (1D) chains of MX_3 prisms which do not possess detrimental dangling bonds and functional groups commonly found in TMDs. The absence of such edge effects suggests TMTs will maintain desirable electronic properties as the channel width scales down, making TMTs suitable materials for electronic device size reduction [16, 19, 29, 44, 45].

TMTs also have promising semiconductor properties, with a band gap comparable to that of silicon (1.1 eV) in the case of TiS_3 [34, 46]. Calculations for TiS_3 find the band gap to be robust, independent from layer thickness, vertical strain [35], and ribbon width [34]. Furthermore, electron mobility along the TiS_3 chains was predicted to be $\sim$10 000 cm^2 Vs^{-1} [27]. Although experimental electronic measurements have

revealed field-effect mobilities in the 1–50 cm^2 $V^{-1}s^{-1}$ range [16, 17, 29, 36–40], ON/OFF ratios of $\sim$10^3 [18], and the sub-threshold swing (S) values of up to $\sim$44 V dec^{-1} [16]. Low experimental mobility is still an issue and the origins of the low mobility may be due to phonon scattering as recently suggested [18] rather than device contact issues [40], yet TiS_3 been gaining attention from a number of researchers. Other properties of TiS_3 in devices have been demonstrated including a model pn-junction constructed of a TiS_3 monolayer [24] that showed promising negative differential resistance and diode rectification behavior. With these device properties, TiS_3 appears to be a promising electronic material that can be positively compared with other more intensively studied members of the TMD family. While phototransistors based on TiS_3 [29], ZrS_3 [25], and HfS_3 [26] have been previously discussed, demonstration of a spin polarized photocurrent is absent. Yet, if spin–orbit coupling is turned on, within the 2D semiconductor channel, new functionality is added.

In this study, we present compelling evidence for chiral effects in $TiS_3(001)$ crystals. Our results strongly suggest the existence of symmetry-protected photocurrent in the plane of the quasi-1D $TiS_3(001)$ crystals. This is distinct from the spin–orbit splitting in the electronic bands in the related MX_2Y (X$\neq$Y=S, Se) Janus 2D monolayers perpendicular to the plane [47].

2. Results and discussion

The x-ray diffraction (XRD) measurements, shown in supporting information (figure S1), indicate that the TiS_3 nano-whiskers conform to a monoclinic structure, with space group: $P2_1/m$, and lattice constants $a = 4.849$ Å, $b = 3.326$ Å, $c = 8.801$ Å and a cant angle of $\beta = 97.3°$ in agreement with previous studies, but slightly different from earlier reported studies values of: $a = 4.949$ Å, $b = 3.379$ Å, $c = 8.748$ Å, and cant angle of $\beta = 97.62°$ [16, 36]; $a = 4.973$ Å, $b = 3.433$ Å, $c = 8.714$ Å can't angle of $\beta = 97.74°$ [39]; and $a = 4.958$ Å, $b = 3.4006$ Å, $c = 8.778$ Å, and $\beta = 97.32°$ [48]. This data suggests that the bulk crystal is centrosymmetric, but the surface cannot possess inversion symmetry as $\beta \neq 90°$.

Indeed, the presence of broken symmetry at the surface such that the surface exhibits a non-centrosymmetric environment, as compared to the centrosymmetric bulk crystal, allows for the possibility of spin–orbit coupling of the surface weighted electronic structure. Spin–orbit coupling of the surface weighted electronic structure, in semiconductors, can heavily influence the band dispersion and optical properties and lead to symmetry protected spin current transport properties. In previous studies [41, 42], measurements of the valence band energy-momentum dispersion in $TiS_3(001)$ along $\bar{\Gamma}-\bar{Y}$ and along $\bar{\Gamma}-\bar{B}$ indicate that although the crystal nominally exhibits $P2_1/m$ symmetry, the surface Brillouin zone lacks mirror plane inversion symmetry, in agreement with the hypothesis produced from the XRD analysis. The absence of the inversion symmetry at the surface is indicated in the constant energy contour photoemission intensity plots [42] and in detailed analysis of the crystal structure (i.e. a non rectilinear

cant angle) that suggests an absence of perfect mirror symmetry at the surface when travelling along the critical points. Additionally, the same study [41] indicated that the band structure is highly anisotropic as is expected, in other words the band structure along the chains (*b* direction) differs from the band structure across the chains (*a* direction). The lack of mirror plane inversion symmetry at the surface suggests, as noted above, that there should be some spin–orbit coupling in the valence band structure [46, 47, 49].

There are several calculations of the band structure for this system, [27–29, 33, 41, 47, 50] but key is that the experimental effective masses have been determined. Indeed, much of the theoretical modeling along with the experimentally measured band structures indicate that the top of the valence band is composed of the S $3p_x$ and Ti $3d_{xz}$ orbitals while the bottom of the conduction band is composed of hybridized Ti 3d and S 3p orbitals with large Ti 3d weighting [50, 51].

High resolution angle-resolved photoemission, taken along the chain direction, as indicated in figure 1(a), provides evidence of the predicted [27, 38, 39, 41] heavy mass and light mass carrier bands at the top of the valence band along the high symmetry $\bar{\Gamma}$–$\bar{Y}$ direction, as the experimental band structure is shown in figures 1(b) and (c). This direction is coincident with the *b* direction in the real space, i.e. the propagation direction of the S–S chains of the nano-whiskers, Parabolic fits of the valence bands indicate the effective hole mass from the heavy hole band and light hole band are $m^*_{hh} = -0.84 \pm 0.03\ m_e$ and $m^*_{lh} = -0.21 \pm 0.02\ m_e$, respectively. The heavy hole mass agrees with values determined in our previous work [38, 42, 43] and with theoretical explanations [27, 38, 39, 41], as noted above. The energy separation, ΔE, between the heavy and light hole bands is $\Delta E = 0.07$ eV. The heavy and light hole bands have contributions from the sulfur $3p_x$, $3p_y$, $3p_z$ and titanium $3d_{xz}$ states [50]. Within instrument resolution there is no direct evidence of appreciable spin–orbit splitting from the electronic band structure, but this does not negate its existence. If there is appreciable spin–orbit coupling in the valence band then the possibility of producing a symmetry protected spin-polarized photocurrent exists [1–6, 52–55].

One way to explore the influence of spin–orbit coupling and chiral effects generally is through scanning photocurrent microscopy (SPCM) using circularly polarized light. SPCM is an *in-situ* technique capable of spatially resolving the in-plane photocurrent response of a field effect transistor (FET) device, here with a spatial resolution on the order of approximately 460 nm. SPCM is well known for its ability to extract information in photosensitive materials related to interfacial band bending between the FET semiconductor channel and the electrodes, as well as the dynamics of charge generation, and the spatial distribution of the induced photocurrent [29, 54, 56–63]. The SPCM experimental geometry is shown in figure 2(a) for the TiS$_3$ phototransistor channel and described in the methods section. The TiS$_3$ back gated phototransistor channel is approximately 4 μm long, 10 nm in height, and 80 nm in width, as indicated by the atomic force microscopy topography image, shown in the inset of figures 3(a) and S2. Before measuring photocurrent response in the transistors, electronic transport measurements were performed without incident light in
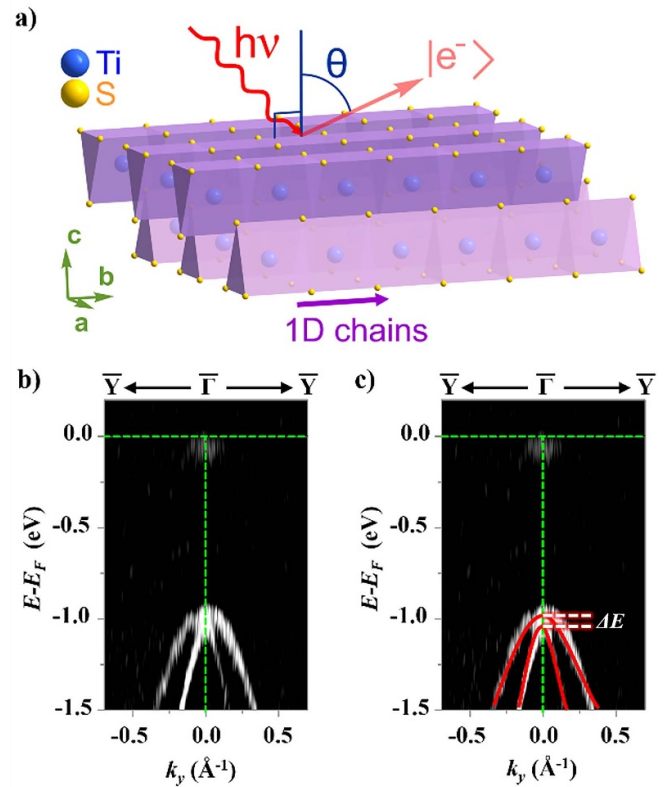

Figure 1. (a) Schematic of nanoARPES taken along the chain direction of TiS$_3$ (001) nano-whiskers, (b) nanoARPES band dispersion of the valence band maximum along $\bar{\Gamma}$–$\bar{Y}$ direction of TiS$_3$(001) indicating heavy and light mass carrier bands at the top of the valence band, and (c) same data as in (b) with fitting curves (solid red) for heavy mass and light mass bands.

order to extract device characteristics of the TiS$_3$ FET, as shown in figure 2(b). The profiles for the dark drain-source current (I_{DS}) versus gate bias (V_G) at low applied drain-source bias (V_{DS}), illustrated in figure 2(b), indicate an n-type material at the contact interface. The n-type behavior is expected from the placement of the valence band maximum [42–44], as seen in figure 1(c), and the transistor characteristics [16, 17, 19, 26–28, 30, 36, 39, 45]. The profiles for dark I_{DS} versus low V_G at high applied V_{DS}, see supporting information, indicate that the Ti/Au contacts exhibit an extremely small Schottky barrier due to an almost completely linear trend in the *I–V* curve. An electron mobility, in the range of 1.2–6 cm^{2}V^{-1} s^{-1}, was estimated from the transfer curves, which is consistent with previously reported mobilities [16, 17, 29, 36–38, 40]. It has been suggested that phonon effects have a major role in reducing the mobility [38, 64], but also in enhancing chirality [55]. Photoinduced strain generation is also known but are unlikely to be sufficiently large to cause the effects seen here [55].

A typical photocurrent image using non-polarized light, for zero bias ($V_{DS} = 0$) and no gate voltage ($V_G = 0$) is shown in figure 3(a). A photocurrent is clearly evident in the TiS$_3$ semiconductor channel near the source and drain electrodes, upon laser illumination. Photocurrent measurements
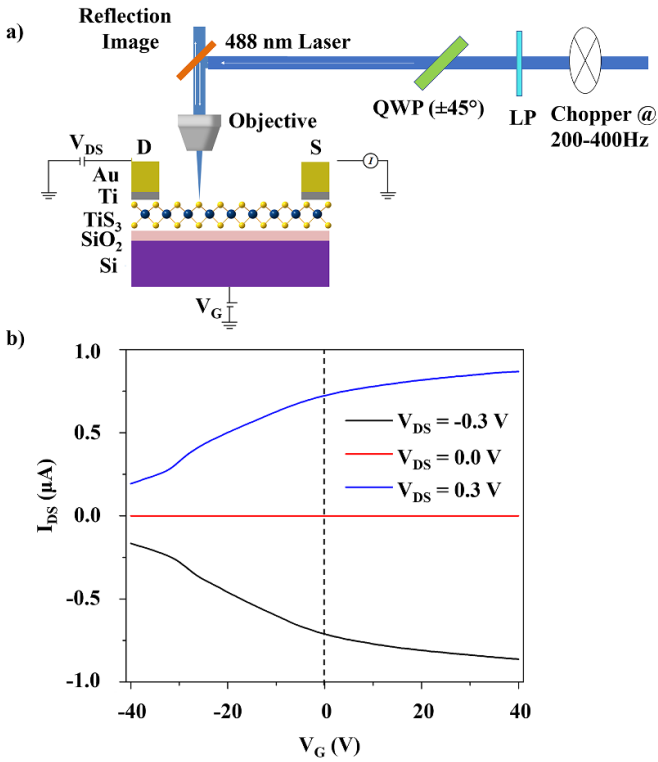
Figure 2. (a) Schematic of scanning photocurrent microscopy on a TiS$_3$ (001) phototransistor using linear polarizer (LP) and quarter wave plate (QWP) to produce right and left circularly polarized light and (b) dark (no illumination) transfer curves indicating behavior of I_{DS} versus V_G.

with non-polarized light and changing photon intensity, indicate an asymmetry in the photocurrent direction, especially at low incident light intensities, as shown in figure 3(b). At a light intensity of 10.3 μW, the black curve in figure 3(b), the asymmetry is most noticeable. Within the semiconductor channel, (at $\approx$ 6 μm in figure 3(b)) near the electrode the photocurrent generated has a higher intensity than near (at $\approx$ 2 μm in figure 3(b)) the opposite electrode, where the generated photocurrent is negligible. As the intensity increases from 10.3 μW to 59 μW (blue curve) the directional asymmetry in the generated photocurrent begins to diminish, although still present. In brief, the ratio between the left and right photocurrents along the TiS$_3$ semiconductor channel is reduced with increasing light intensity. The asymmetry is also present and reverses when the drain-source bias is reversed. Additionally, the magnitude of both the right and left photocurrent peaks scale linearly with incident light intensity, see supporting figure S4, which is characteristic of a photocurrent unperturbed by contact problems [52], suggesting the asymmetry is not a contact issue. This is consistent with the observation that gold contacts to TiS$_3$ are largely Ohmic [28, 30].

An asymmetry in the photocurrent is most likely due to a combination of the photothermoelectric effect and photovoltaic effect [65]. The origins of the photoresponse and the resulting electronic transport in TiS$_3$ have been reported to be solely due to the photovoltaic effect [29]. In the current devices it is difficult to distinguish the dominant effect, either

photovoltaic or photothermoelectric effects, but the data suggests both are present in the system. The photothermoelectric effect, also known as the Seebeck effect, is photoexcitation of carriers due to a photothermal voltage produced by a temperature gradient across the interface of two materials with different Seebeck coefficients [66]. The gold electrode and the TiS$_3$ conduction channel have different Seebeck coefficients and upon illumination, with the small laser beam profile, will produce a photothermal voltage due to local heating from the light source. The photothermal voltage acts to drive the carriers along the conduction channel. Although the temperature change produced at the surface by the light source will be small, on the order of a few Kelvin, it may nonetheless be sufficient to produce an photothermal voltage [29]. The lack of a photocurrent sign change as the gate bias changes from positive to negative, see figure S5, as is typical for the photovoltaic effect, is indicative of the presence of the photothermoelectric effect [64]. The magnitude of the photothermoelectric effect scales with an increasing temperature difference and thus as the photon intensity increases we should expect to see increased photocurrent at both ends of the device, as we see in figure 3(b), dramatically reducing the photocurrent asymmetry along the channel near the electrode interface.

The photovoltaic effect is the separation of photoexcited electron–hole pairs via a built-in electric field located at the interface of a p–n junction or at a Schottky junction [66]. In the present case, we know the interface between the electrode and the TiS$_3$ conduction channel may possess a small contact barrier, see figure S3, although Au contacts are generally expected to be Ohmic [38, 40]. The photovoltaic effect will also scale with increasing photon intensity and result in increased photocurrent as shown in figure 3(b). More direct evidence for the presence of the photovoltaic effect is seen in figure 3(c), through the positive to negative photocurrent sign change with changing drain-source bias, typical of the photovoltaic effect in phototransistors. Moreover, for the photovoltaic response from a metal/semiconductor junction, the position of the maximum photocurrent is expected to shift with the gate voltage. As the gate bias increases this effectively increases the depletion width of the Schottky barrier and so you would expect to see movement of the peaks inward toward the channel and away from the electrode [66], as seen in figure S5. From these observations it is clear both the photovoltaic and photothermoelectric effects are present in our devices.

The asymmetrical photocurrent effect has been reported elsewhere for symmetry protected photocurrents [5], where the reduced asymmetry at higher incident light intensity is believed to be due to a thermal heating effect. In fact, similar photocurrent asymmetry, to that seen here, has been seen in atomically thin WS$_2$ FETs [6] and in MoS$_2$ FETs [1–5]. Even minimal heating of the surface would diminish the effects of the spin–orbit coupling within the valence band and thus pose problems for optical-spintronic device applications where higher photon intensity could be used to create larger photocurrents.

Chiral effects require a breaking of inversion symmetry which leads to excitation that favors one circular polarization over the other [1]. This is satisfied by the TiS$_3$ crystal, as
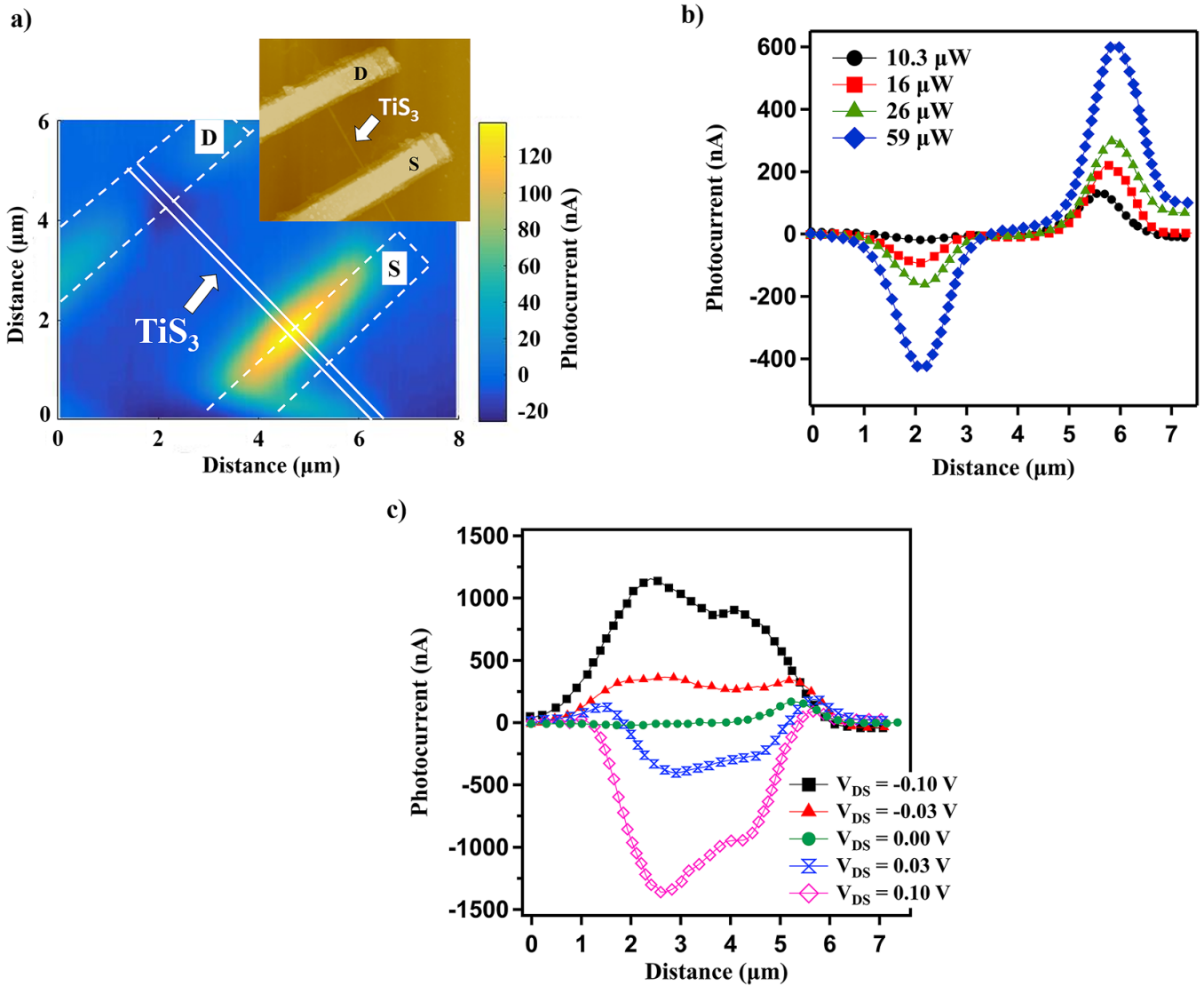
Figure 3. (a) The scanning photocurrent microscopy image of FET at light intensity of 10.3 μW indicating asymmetry of photoinduced current intensity near contacts. The white dashed line indicates the electrode edges and the white solid lines are the TiS$_3$ conduction channel where the line-cuts were taken in figure (b), inset: AFM image of the FET structure, (b) incident photon intensity dependence of photocurrent along channel, $V_G = 0$ V, $V_{DS} = 0$ V and (c) drain-source bias dependence of photocurrent versus position along the TiS$_3$ FET conduction channel, $V_G = 0$ V. All light used in the above measurements was non-polarized.

indicated by XRD and experimentally realized by the inclusion of a linear polarizer and a quarter wave plate to induce circular polarization, described in the methods section. The photoexcitation from TiS$_3$(100) is sensitive to the circular polarization of the incident light, producing a directional photocurrent, as illustrated in figure 4.

The absolute value of the photocurrent, for 100 μW incident circularly polarized light, is plotted as a function of distance along the device conduction channel in figure 4 which shows a polarization dependence of the photocurrent for the phototransistor. Notice there is a marked difference in the photocurrent intensity upon switching the polarization from right (blue) to left (red) circularly polarized. This dichroitic property is not due to the polycrystalline metal contacts, as even with contact problems (asymmetry, etc) producing a favored current flow between the contacts it would be independent of light polarization. Currently, substrate effects cannot be excluded by the data. It is expected that random defect and substrate contributions would only serve to diminish the chiral effects and mobility. It is plausible that the substrate has significant effects, such as the introduction of defect/impurity scattering and loss of inversion symmetry, enough to enhance the spin–orbit coupling but it would need to perturb more than just the interface TiS$_3$ layer. Defects would tend to be anisotropically distributed diminishing any possibility that this contributes to the observed chiral effects [67]. This is expected as the introduction of defects would not necessarily allow for the preservation of symmetry. In the extreme limit, as in an amorphous material, there is no inversion symmetry but also no net chirality. It is acknowledged that this is not the only way to lose mobility as phonons could also contribute to the loss of mobility.
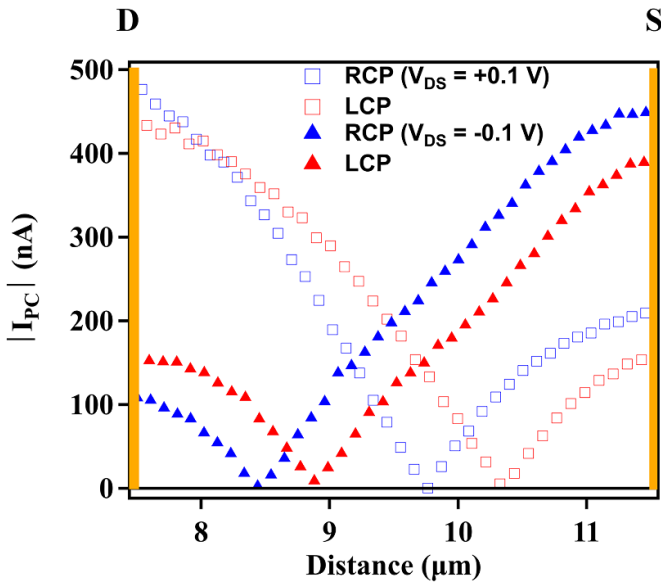
Figure 4. Absolute value of background corrected photocurrent between the electrodes, blue(red) is with right(left) circularly polarized light, solid triangle ($V_{DS} = -0.1$ V), open squares ($V_{DS} = +0.1$ V), the gold rectangles near the plot edges represent the position of the drain (D) and source (S) electrodes, $V_G = 0$ V.

This light polarization dependent switching of the photocurrent is more comparable to the circular photogalvanic effect [68] and the circular photon drag effect [69], although typically an applied bias is not present. Theoretically, both of these circular polarization dependent effects suggest the presence of strong spin–orbit coupling. Indeed, within the conduction channel the magnitude and polarization dependence of the photocurrent are observed to change with a change in bias direction similar to bipolar spin diode behavior [70], as shown in figure 4. At $V_{DS} = -0.1$ V (solid triangles), the photocurrent produced with left circularly polarized light (red) dominates near the drain electrode, whereas the photocurrent produced with right circularly polarized light (blue) dominates near the source electrode. The opposite trend is true when the bias switches from $V_{DS} = -0.1$ V to $+0.1$ V. We believe the bias dependent switching is due to symmetry considerations. As mentioned earlier, in a previous study [42] we determined that not only is there a lack of inversion symmetry in the band dispersion but also the band structure is anisotropic such that a preferred carrier direction along the chains rather than across the chains is present. The bias direction and change in weighted intensity is similar to the anomalous hall effect where opposite spins experience asymmetric scattering due to the effective spin–orbit coupling of the electron [71]. Interestingly, a bias dependence of the spin current was shown in calculations of $F:TiS_3/Li:TiS_3$ p–n heterojunctions, although the weighted intensity does not switch from spin-up to spin-down when the bias is reversed, which is attributed to a dominant spin-up quantum mechanical transmission function near the Fermi level [24]. Although the linear polarization dependent photocurrent in TiS_3 has been observed previously [50], this is the first report of circular polarization dependence of the photocurrent and helps support the existence of

spin–orbit coupling at the surface. Chiral optical effects are very much consistent with the very specific band symmetries of TiS_3 noted elsewhere [50]. We note that TiS_3 is not the only chiral 2D material as chiral tellurium is also known [54]. The system that TiS_3 most resembles are the dichalcogenides and chiral tellurium as in [55, 72–75], although these systems exhibit chiral effects, this is not the result of optical transitions between electronic state but rather transitions between phonon bands.

3. Conclusion

In summary, this study has shown that through inversion symmetry chiral effects appear at the surface of a $TiS_3(001)$ photo conduction channel. This is evident from the crystal symmetry measured with XRD and the photocurrent generated with circularly polarized light. The preferential direction for the photocurrent in TiS_3, one that depends on the circular polarization, suggests not only the presence of chirality, but also a loss of crystal symmetry and ultimately suggests the presence of spin–orbit coupling. A preferential direction for the photocurrent is expected for the TMDs [1–6], and is similar to the topologically protected photocurrents seen in topological insulators, namely Bi_2Se_3 [52, 76], $(Bi_{0.5}Sb_{0.5})_2Te_3$ [53], and $BiSbTeSe_2$ [76]. The presence of anisotropy in the band structure suggests that symmetry protected spin-polarized photocurrent will occur and this will be useful for spintronic device applications, especially in situations which call for low power and high data egress [77]. The development of a TMT-field-effect phototransistor means that the TMT-FET has application as an optical sensor, while retaining potential utility of these devices for logic computation.

4. Experimental methods

TiS_3 (001) micro-whiskers were grown following previous work [16, 25, 36–38, 40, 42, 43, 50, 78–81], via the direct reaction of titanium and sulfur. Ti foil (0.1 g, 0.25 mm thick) and S powder (0.2 g) are sealed in an evacuated (pressure $\approx$ 200 mTorr) quartz ampule and annealed in a tube furnace for 5 d at temperatures up to 550 °C.

TiS_3 nano-whiskers were mechanically exfoliated from the micro-whiskers and then transferred to a Si substrate with an insulating top layer of SiO_2. Metal contacts consisting of 5 nm of Ti or Cr followed by 50 nm of Au were placed, roughly 4 μm apart, over a single nano-whisker using electron beam lithography, photolithography, and physical vapor deposition methods.

Nanospot angle resolved photoemission spectroscopy (nanoARPES) measurements were performed on the Antares beamline of the synchrotron Soleil [82], Paris using a MBS deflection analyzer, with an angular and energy resolution of $\sim$0.2° and $\sim$10 meV, respectively. The small spot size of $\sim$350 nm allows for precise positioning and location of small samples as well as the correct alignment required to perform the angle resolved measurements [83, 84].

SPCM was performed at the Center for Functional Nanomaterials at Brookhaven National Laboratory with a scanning photocurrent microscope built on an inverted Olympus IX 81 microscope equipped with a $50\times$, 0.5 numerical aperture lens (Olympus America), a raster scanning stage (N-Point NPXY400), and a single photon counting avalanche photodiode detector (Tau SPAD Picoquant Germany) for reflection imaging. A spatially resolved photocurrent image is simultaneously generated with a reflection image of the device by using a 488 nm solid state laser (Coherent Sapphire 100), the incident light impinges upon the device perpendicularly after reflection from a dichroic mirror. Electrical signals from devices are measured by a low-noise current amplifier (Femto DLPCA), converted into voltage by a lock-in amplifier (Stanford Research 830) and read by a SoftDB scanning probe microscope controller equipped with GSXM software (Gnome X Scanning Microscopy). The circular polarization of the light source was achieved through the use of a linear polarizer followed by a quarter wave plate at positive or negative $45°$ with respect to the linear polarizer.

XRD measurements were performed in air at room temperature with a Rigaku Smart Lab diffractometer equipped with a Cu Kα source, $\lambda = 1.54$ Å.

Data availability statement

The data that support the findings of this study are available upon reasonable request from the authors.

Acknowledgments

Conflict of interest

The authors declare no conflict of interest.

ORCID iDs

Simeon J Gilbert ⓘ https://orcid.org/0000-0003-0402-9305
Alexey Lipatov ⓘ https://orcid.org/0000-0001-5043-1616
Alexander Sinitskii ⓘ https://orcid.org/0000-0002-8688-3451
Maria C Asensio ⓘ https://orcid.org/0000-0001-8252-7655
Peter A Dowben ⓘ https://orcid.org/0000-0002-2198-4710
Andrew J Yost ⓘ https://orcid.org/0000-0002-6220-7520

References

[1] Wu L H and Hu X 2015 *Phys. Rev. Lett.* **114** 223901
[2] Cao T *et al* 2012 *Nat. Commun.* **3** 885
[3] Xiao D, Liu G-B, Feng W, Xu X and Yao W 2012 *Phys. Rev. Lett.* **108** 196802
[4] Kormányos A, Burkard G, Gmitra M, Fabian J, Zólyomi V, Drummond N D and Fal'ko V 2014 *2D Mater.* **2** 022001
[5] Zeng H, Dai J, Yao W, Xiao D and Cui X 2012 *Nat. Nanotechnol.* **7** 490
[6] Xie L and Cui X 2016 *Proc. Natl Acad. Sci.* **113** 3746
[7] Przybylski H, Baalmann A, Borstel G and Neumann M 1983 *Phys. Rev.* B **27** 6669
[8] Dubois S M M, Lopez-Bezanilla A, Cresti A, Triozon F, Biel B, Charlier J C and Roche S 2010 *ACS Nano* **4** 1971
[9] Jensen S A, Ulbricht R, Narita A, Feng X, Müllen K, Hertel T, Turchinovich D and Bonn M 2013 *Nano Lett.* **13** 5925
[10] Kumar P, Skomski R, Manchanda P, Kashyap A and Dowben P A 2014 *Curr. Appl. Phys.* **14** S136
[11] Wimmer M, Adagideli İ, Berber S, Tománek D and Richter K 2008 *Phys. Rev. Lett.* **100** 177207
[12] Han M Y, Brant J C and Kim P 2010 *Phys. Rev. Lett.* **104** 056801
[13] Wang X, Ouyang Y, Jiao L, Wang H, Xie L, Wu J, Guo J and Dai H 2011 *Nat. Nanotechnol.* **6** 563
[14] Mlinar V 2017 *Phys. Chem. Chem. Phys.* **19** 15891
[15] Dong L, Wang J, Namburu R, O'Regan T P, Dubey M and Dongare A M 2015 *J. Appl. Phys.* **117** 244303
[16] Lipatov A, Wilson P M, Shekhirev M, Teeter J D, Netusil R and Sinitskii A 2015 *Nanoscale* **7** 12291
[17] Island J O, Biele R, Barawi M, Clamagirand J M, Ares J R, Sánchez C, Van Der Zant H S J, Ferrer I J, D'Agosta R and Castellanos-Gomez A 2016 *Sci. Rep.* **6** 1
[18] Lipatov A *et al* 2018 *ACS Nano* **12** 12713
[19] Dhingra A *et al* 2020 *Semicond. Sci. Technol.* **35** 065009
[20] Butler S Z *et al* 2013 *ACS Nano* **7** 2898
[21] Chhowalla M, Shin H S, Eda G, Li L J, Loh K P and Zhang H 2013 *Nat. Chem.* **5** 263
[22] Jariwala D, Sangwan V K, Lauhon L J, Marks T J and Hersam M C 2014 *ACS Nano* **8** 1102
[23] Wang Q H, Kalantar-Zadeh K, Kis A, Coleman J N and Strano M S 2012 *Nat. Nanotechnol.* **7** 699
[24] Iyikanat F, Senger R T, Peeters F M and Sahin H 2016 *ChemPhysChem* **17** 3985

[25] Tao Y R, Wu J J and Wu X C 2015 *Nanoscale* **7** 14292
[26] Xiong W-W, Chen J-Q, Wu X-C and Zhu J-J 2014 *J. Mater. Chem.* C **2** 7392
[27] Dai J and Zeng X C 2015 *Angew. Chem., Int. Ed.* **54** 7572
[28] Jin Y, Li X and Yang J 2015 *Phys. Chem. Chem. Phys.* **17** 18665
[29] Island J O, Buscema M, Barawi M, Clamagirand J M, Ares J R, Sánchez C, Ferrer I J, Steele G A, van der Zant H S J and Castellanos-Gomez A 2014 *Adv. Opt. Mater.* **2** 641
[30] Ferrer I J, Maciá M D, Carcelén V, Ares J R and Sánchez C 2011 *Energy Proc.* **22** 48
[31] Dai J, Li M and Zeng X C 2016 *Wiley Interdiscip. Rev. Comput. Mol. Sci.* **6** 211
[32] Island J O *et al* 2017 *2D Mater.* **4** 22003
[33] Liu S, Xiao W, Zhong M, Pan L, Wang X, Deng H-X, Liu J, Li J and Wei Z 2018 *Nanotechnology* **29** 184002
[34] Kang J, Sahin H, Ozaydin H D, Senger R T and Peeters F M 2015 *Phys. Rev.* B **92** 1
[35] Kang J and Wang L-W 2016 *Phys. Chem. Chem. Phys.* **18** 14805
[36] Cui Q, Lipatov A, Wilt J S, Bellus M Z, Zeng X C, Wu J, Sinitskii A and Zhao H 2016 *ACS Appl. Mater. Interfaces* **8** 18334
[37] Finkman E and Fisher B 1984 *Solid State Commun.* **50** 25
[38] Randle M *et al* 2019 *ACS Nano* **13** 803
[39] Island J O *et al* 2015 *Adv. Mater.* **27** 2595
[40] Gilbert S J, Lipatov A, Yost A J, Loes M J, Sinitskii A and Dowben P A 2019 *Appl. Phys. Lett.* **114** 101604
[41] Silva-Guillén J A, Canadell E, Ordejón P, Guinea F and Roldán R 2017 *2D Mater.* **4** 025085
[42] Yi H *et al* 2018 *Appl. Phys. Lett.* **112** 052102
[43] Yi H, Gilbert S J, Lipatov A, Sinitskii A, Avila J, Abourahma J, Komesu T, Asensio M C and Dowben P A 2020 *J. Phys.: Condens. Matter* **32** 29LT01
[44] Empante T A *et al* 2019 *Nano Lett.* **19** 4355
[45] Galiy P V *et al* 2019 *2019 IEEE 2nd Ukrainian Conf. Electr. Comput. Eng. UKRCON 2019—Proc.* p 679
[46] Dresselhaus G, Kip A F and Kittel C 1954 *Phys. Rev.* **95** 568
[47] Ahammed R, Jena N, Rawat A, Mohanta M K, Sharma D and Sarkar A D 2020 *J. Phys. Chem.* C **124** 21250–60
[48] Furuseth S, Brattås L and Kjekshus A 1975 *Acta Chem. Scand.* A **29** 623
[49] Rashba E 1960 *Sov. Phys.-Solid State* **2** 1109
[50] Gilbert S J *et al* 2020 *ACS Appl. Mater. Interfaces* **12** 40525
[51] Gilbert S J, Yi H, Paudel T, Lipatov A, Yost A J, Sinitskii A, Tsymbal E Y, Avila J, Asensio M C and Dowben P A 2022 *J. Phys. Chem.* C **126** 17647–55
[52] McIver J W, Hsieh D, Steinberg H, Jarillo-Herrero P and Gedik N 2012 *Nat. Nanotechnol.* **7** 96
[53] Qu D-X, Che X, Kou X, Pan L, Crowhurst J, Armstrong M R, Dubois J, Wang K L and Chapline G F 2018 *Phys. Rev.* B **97** 045308
[54] Ubrig N, Jo S, Berger H, Morpurgo A F and Kuzmenko A B 2014 *Appl. Phys. Lett.* **104** 171112
[55] Jnawali G *et al* 2020 *Nat. Commun.* **11** 3991
[56] Li M, Chen J S, Routh P K, Zahl P, Nam C Y and Cotlet M 2018 *Adv. Funct. Mater.* **28** 1707558
[57] Xia F, Mueller T, Golizadeh-Mojarad R, Freitage M, Lin Y M, Tsang J, Perebeinos V and Avouris P 2009 *Nano Lett.* **9** 1039
[58] Allen J E, Perea D E, Hemesath E R and Lauhon L J 2009 *Adv. Mater.* **21** 3067
[59] Graham R, Miller C, Oh E and Yu D 2011 *Nano Lett.* **11** 717
[60] Jo M-H, Cho Y-J, Kang K, Kim C-J and Lee H-S 2010 *Nano Lett.* **10** 2043
[61] Ahn Y, Dunning J and Park J 2005 *Nano Lett.* **5** 1367
[62] Dorfmüller J, Kern K, Lee E J H, Mews A, Balasubramanian K, Burghard M, Fu N and Vogelgesang R 2007 *Small* **3** 2038
[63] Wu C C, Jariwala D, Sangwan V K, Marks T J, Hersam M C and Lauhon L J 2013 *J. Phys. Chem. Lett.* **4** 2508
[64] Dhingra A, Lipatov A, Sinitskii A and Dowben P A 2021 *J. Phys.: Condens. Matter* **33** 434001
[65] Zhang Y, Li H, Wang L, Wang H, Xie X, Zhang S L, Liu R and Qiu Z J 2015 *Sci. Rep.* **5** 1
[66] Castellanos-Gomez A, Buscema M, van der Zant H S J and Steele G A 2016 *2D Materials for Nanoelectronics, Chapter 10: Optoelectronics, Mechanical Properties and Strain Engineering in MoS2* (Boca Raton, FL: Taylor & Francis)
[67] Arsentev M, Missyul A, Petrov A V and Hammouri M 2017 *J. Phys. Chem.* C **121** 15509
[68] Asnin V M, Bakun A A, Danishevskii A M, Ivchenko E L, Pikus G E and Rogachev A A 1979 *Solid State Commun.* **30** 565
[69] Shalygin V A, Moldavskaya M D, Danilov S N, Farbshtein I I and Golub L E 2017 *J. Phys.: Conf. Ser.* **864** 012072
[70] Zeng M, Shen L, Zhou M, Zhang C and Feng Y 2011 *Phys. Rev.* B **83** 115427
[71] Nagaosa N, Sinova J, Onoda S, MacDonald A H and Ong N P 2010 *Rev. Mod. Phys.* **82** 1539
[72] Ma J *et al* 2022 *Nat. Commun.* **13** 5425
[73] Londoño-Calderon A, Williams D J, Schneider M M, Savitzky B H, Ophus C, Ma S, Zhu H and Pettes M T 2021 *Nanoscale* **13** 9606–14
[74] Li J, Yang W, Liu J-T, Huang W, Li C and Chen S-Y 2017 *Phys. Rev.* B **95** 035308
[75] Wittmann B *et al* 2010 *Semicond. Sci. Technol.* **25** 095005
[76] Liu Y *et al* 2018 *Nat. Commun.* **9** 2492
[77] Dowben P A, Binek C, Zhang K, Wang L, Mei W-N, Bird J P, Singisetti U, Hong X, Wang K L and Nikonov D 2018 *IEEE J. Explor. Solid-State Comput. Devices Circuits* **4** 1
[78] Brattås L, Kjekshus A, Krogh-Moe J, Songstad J and Pilotti Å 1972 *Acta Chem. Scand.* **26** 3441
[79] Kikkawa S, Koizumi M, Yamanaka S, Onuki Y and Tanuma S 1980 *Phys. Status Solidi* **61** K55
[80] Haraldsen H, Kjekshus A, Røst E, Steffensen A and Munch-Petersen J 1963 *Acta Chem. Scand.* **17** 1283
[81] Lévy F and Berger H 1983 *J. Cryst. Growth* **61** 61
[82] Avila J, Razado-Colambo I, Lorcy S, Lagarde B, Giorgetta J L, Polack F and Asensio M C 2013 *J. Phys.: Conf. Ser.* **425** 192023
[83] Avila J and Asensio M C 2014 *Synchrotron Radiat. News* **27** 24
[84] Avila J, Razado I, Lorcy S, Fleurier R, Pichonat E, Vignaud D, Wallart X and Asensio M C 2013 *Sci. Rep.* **3** 1